Chapter 17
Acoustic Signal for Femtosecond Filament Plasma Grating Characterization in Air

Daniil E. Shipilo, Vladislav V. Pankratov, Nikolay A. Panov, Vladimir A. Makarov, Andrei B. Savel'ev and Olga G. Kosareva

Abstract We have designed the physical model and numerical algorithm for the simulations of acoustic wave propagation from the source induced by relaxation of a femtosecond plasma grating formed by two crossing filaments in atmospheric air. The model is based on the wave equation with the wave velocity depending on the transverse temperature variation. The algorithm is based on the fine resolution ($\approx 2\,\mu$m) numerical grid employed for the description of the plasma channel substructures in the course of femtosecond filamentation. We have shown that the femtosecond plasma grating emits the superposition of two acoustic signals after plasma recombination. One acoustic signal is represented by an isotropic cylindrical waveform with the characteristic spatial scale equal to the filament diameter (100–200 μm) while the other has the spatial scale equal to the plasma grating period in the range 20−40 μm. This second wave propagates in the direction parallel to the axis of plasma grating modulation. Based on the simulations, we suggested the noninvasive method for the plasma grating period and the beam convergence angle detection.

17.1 Introduction

Diagnostics of the high-intensity zone produced by ultrashort laser pulse filamentation [1–3] is a nontrivial task requiring specially designed setup, since almost any material inserted into a high-intensity beam will be destroyed. The example of such invasive diagnostics is insertion of a glass plate into the terawatt peak power 800 nm

D. E. Shipilo · V. V. Pankratov · N. A. Panov · V. A. Makarov · A. B. Savel'ev · O. G. Kosareva (✉)
Faculty of Physics and International Laser Center, Lomonosov Moscow State University, 1, bld. 62 Leninskiye gori, Moscow 119991, Russia
e-mail: kosareva@physics.msu.ru

D. E. Shipilo · V. V. Pankratov · N. A. Panov · O. G. Kosareva
Lebedev Physical Institute of the Russian Academy of Sciences, 53 Leninskiy prospect, Moscow 119991, Russia

O. G. Kosareva
Institute of Modern Optics, Nankai University, 300350 Tianjin, China

K. Yamanouchi et al. (eds.), *Progress in Photon Science*, Springer Series in Chemical Physics 119, https://doi.org/10.1007/978-3-030-05974-3_17

beam and identification of the system of multiple rings surrounding the filament by the ablation from the glass surface [4]. Quantitatively, the invasive diagnostics might be performed by reflecting the beam from the white paper screen or a wedge and sending a small part of the overall energy to a CCD for transverse and temporal measurements (see, e.g., [5–7]). Such type of invasive measurements can be performed at a certain propagation position because the measurement destroys the filament. The noninvasive longitudinal diagnostics of femtosecond filament is done by means of ICCD camera and the UV filter in front of it in order to observe the nitrogen fluorescence from aside [8, 9]. With this technique the nitrogen fluorescence signal is resolved in the longitudinal direction of the pulse propagation but integrated over the filament transverse section.

In parallel with filament study by optical methods, photoacoustic methods were employed for filament characterization [10, 11]. The sensitivity of the photoacoustic method is high enough to detect the energy deposition into air in the prefilamentation regime without plasma generation. The amount of energy absorbed into molecular gases of air is relatively low (the peak intensity is below 10^{12} W/cm^2), however the acoustic signal was securely detected already at 1-mJ energy of 80-fs 795-nm initial pulse in [11]. The typical time of acoustic wave formation is $d/c_0 \approx 0.3\,\mu$s, where $d \approx 100\,\mu$m is the filament transverse size and $c_0 \approx 340$ m/s is the speed of sound in air. The microphone used in [11] had the bandwidth of 100 kHz. The corresponding temporal resolution was about 10 μs or worse. With this resolution the identification of filament transverse size was not possible, since the detected acoustic waveform characteristic spatial scale was 6.6 mm exceeding the filament diameter and any fine transverse spatial structure within the plasma channel.

The nicely resolved evolution of acoustic wave was observed by performing imaging interferometry for direct measurement of the evolving refractive index profile. The authors used folded wavefront interferometry [12], which measures the 2D phase shift of the probe beam, from which the refractive index perturbation δn is extracted. According to [12] the measured refractive index variation due to air density perturbation in the filament core is $\delta n \approx 10^{-5}$. Taking into account that the refractive index of air at standard temperature and pressure is $n_0 - 1 \approx 2.7 \times 10^{-4}$ [13], which is due to the standard atmospheric density 2.68×10^{19} cm^{-3} or $\rho_0 = 1.3$ kg/m^3, we can estimate the relative density fluctuation $\delta\rho$ due to the plasma-induced heating. Indeed,

$$\frac{\delta\rho}{\rho_0} = \frac{\delta n}{n_0 - 1} = \frac{10^{-5}}{2.7 \times 10^{-4}} \approx 0.04\,. \tag{17.1}$$

Four-filament regular structures produce the acoustic waveguide on the microsecond time scale and the thermal waveguide on the millisecond time scale [14]. Long-lived refractive index perturbations responsible for these guiding structures are analyzed by means of imaging interferometry.

The high-resolution imaging interferometry technique [12, 14] may be complemented by straightforward measurement of air density variation using a wideband piezoelectric transducer [15, 16]. In the experiment [15] the laser beam from 1-TW Ti:Sapphire laser (805 nm, 55 fs, 10 Hz, beam diameter 7 mm FWHM) was focused

by the plane-convex lens with a focal length of 3 m. A single filament was formed if the laser pulse energy was 2.5–3 mJ. To create multiple filaments, the energy of the pulse was increased to 8 mJ. Both optical and acoustic diagnostics were used in each laser shot. The wedge prism was used to direct a small part of the optical radiation after the filament to a CCD camera to visualize the transverse distribution of the beam fluence. The wedge prism was located more than 1 m beyond the focal point of the lens, so it was not damaged by the filament. The acoustic diagnostics included a broadband piezoelectric transducer utilizing a 110-μm-thick polyvinylidene fluoride (PVDF) polymer film (the operating bandwidth is up to 6 MHz) with an operating area 6 mm in diameter. This transducer was placed at a distance of 286 cm from the lens and at a distance of 3–4 mm from the filament. Low acoustic impedance and ability to operate in a wide ultrasonic frequency band are the advantages of PVDF piezoelectric films for detection of optoacoustic signals [17]. The signal from the piezoelectric transducer was amplified by the broadband amplifier with a gain of 12 and recorded using ADC PLX9054 PCI PC card (digitization frequency 500 MHz, 8-bit resolution, Rudnev-Shilyaev Corporation). In a single filament regime acoustic waveform detected by the piezoelectric transducer had one maximum with a characteristic transverse spatial scale of 0.4 μs corresponding to the filament diameter $d \approx 100\,\mu$m. In the multiple filament regime several local maxima were observed with peak-to-peak separation of the order of the filament size $d \approx 100\,\mu$m. So, the acoustic method with the 6 MHz broadband piezoelectric transducer allows one to resolve the multiple filament structure.

The advantage of using this broadband acoustic method [15, 16] is the possibility to perform non-invasive analysis as compared with the transverse beam section registration using a CCD and a wedge. The frequency bandwidth larger than 1 MHz ensures submicrosecond temporal resolution. This high resolution acoustic method requires just one or several detectors and does not require the probe beam or optical scheme adjustment. Indeed, the broadband microphone can be used in outdoor conditions for express analysis of multiple filament structure and energy deposition into the medium. Energy deposition into air in the course of single 800-nm filament regime was studied in [18] and was found to be in the range 1–3% of the initial 800-nm pulse energy of 2–4 mJ. In the multiple filament regime the acoustic method was used to follow the lineic (energy per unit length) energy deposition along the superfilament [19]. For the 800-nm pump pulse of 165 mJ, duration 50 fs and geometrical focusing distance in air of 30 cm, the linear deposited energy per 1 cm was found to be 10 mJ using a sonographic technique. In the regularized superfilamentation regime ensured by merging of 4 filaments produced by the amplitude mask the sonographic method showed the deposition of approximately 0.15 mJ per 1 cm out of 10 mJ of the initial pulse energy [20]. The deposited energy was growing faster than linearly with the initial pulse energy increase [19, 20].

Thus, for the past 4 years the acoustic method in studying single and multiple femtosecond filaments has advanced significantly. It was shown that broadband acoustic detectors can be used to noninvasively analyze both energy deposition and fine structure of the plasma filaments.

In this paper we suggest the method for the noninvasive analysis of the dynamic plasma grating produced by interference of two noncollinearly propagating beams from the same 50 fs, 800 nm pulse with the energy of 1.2 mJ, beam diameter of 8 mm at e^{-2} level and 1 kHz repetition rate [22]. The analysis will be performed numerically in the experimental conditions [22]. According to the suggested method the wideband (more than 6 MHz) piezoelectric transducer is located within the distance of several millimeters from the dynamic plasma grating. We simulate the acoustic wave detected by this wideband transducer. The origin of the acoustic wave is the air density perturbation after the plasma recombination in the grating. The directional diagram and frequency spectrum of the acoustic wave induced by the grating are studied and two characteristic spectral maxima corresponding to the overall plasma width in the filament and the width of one strip of the grating (the grating period) are identified numerically based on the solution of the full wave equation for acoustic signal propagation.

17.2 Numerical Model of Plasma-Induced Acoustic Wave Propagation

We suppose that the medium with the background temperature $\theta_0 = 293$ K has a temperature perturbation $T_0(x, y, z)$ induced by the filament's plasma recombination. We start from the gas dynamics equation system:

$$\begin{cases} \dfrac{\partial \rho}{\partial t} + \nabla(\rho \mathbf{u}) = 0 \\ \rho\left(\dfrac{\partial \mathbf{u}}{\partial t} + (\mathbf{u}\cdot\nabla)\,\mathbf{u}\right) = -\nabla p \\ p = p_0\left(\dfrac{\rho}{\rho_0}\right)^{\gamma} \end{cases} \tag{17.2}$$

where ρ is the air density, p is the air pressure, $\mathbf{u}$ is the flow velocity vector, $p_0 = \rho_0 R\theta_0/\mu$ is the standard atmospheric pressure, $R = 8.31$ J/(K mol), $\mu = 29$ g/mol is the molar mass of air. The dependence $p(\rho)$ corresponds to the adiabatic law with the adiabatic index $\gamma = 1.4$. After linearization with the density perturbation $\rho' = \rho - \rho_0$ as a small parameter, we obtained the wave equation

$$\Delta\xi - \frac{1}{c^2(x, y, z)}\frac{\partial^2 \xi}{\partial t^2} = 0 \tag{17.3}$$

for the medium excitation function [23]:

$$\xi\,(x, y, z, t) = \left[\rho_0 + \gamma\rho'\,(x, y, z, t)\right] \times \left[\theta_0 + T_0\,(x, y, z)\right]\,, \tag{17.4}$$

where the velocity is expressed as

$$c^2 = c_0^2 \left(1 + \frac{T_0}{\theta_0}\right) , \tag{17.5}$$

and $c_0 = \sqrt{(\gamma R \theta_0/\mu)}$ is the speed of sound in the unperturbed medium. Please, note that the function ξ is not directly proportional to the air pressure $p \propto \left[\rho_0 + \rho'\right] \times [\theta_0 + T_0]$ since the density perturbation ρ' is multiplied by the adiabatic index coefficient in (17.4).

Thus, after the plasma recombination with the characteristic time of 10 ns [21], we obtain the extended region with the characteristic spatial scales of the plasma channel size heated above the room temperature by $T_{00} \approx 70$ K, which can be estimated from

$$\frac{5}{2} k_B T_{00} = U_i N_e , \tag{17.6}$$

where $U_i = 12.2$ eV is the ionization potential, $N_e \sim 10^{16}\,\mathrm{cm}^{-3}$ is the filament plasma density and k_B is the Boltzmann constant. The longitudinal size of this extended region exceeds its transverse size by 3 orders of magnitude at least (the ratio of 10 cm to 100 μm). Thanks to this large ratio we can neglect the derivatives along the propagation coordinate z and in (17.3) we retain the transverse Laplacian only:

$$\Delta \approx \Delta_\perp = \frac{\partial^2}{\partial x^2} + \frac{\partial^2}{\partial y^2} . \tag{17.7}$$

For our case of the dynamic plasma grating produced by the interference of two noncollinearly propagating beams [22] we assume that the initial temperature perturbation $T_0(x, y)$ reproduces the shape of the plasma channels in the vicinity of the geometrical focus and remains the same for all positions z along the filament. This shape consists of the Gaussian intensity distribution with the characteristic transverse size of the order of the filament diameter $d = 2a_{fil}$. Moreover, due to the interference of the two beams converging towards each other, the Gaussian intensity distribution is modulated with the period

$$d_{pl} = \frac{\lambda}{\sin \alpha} \tag{17.8}$$

in the plane perpendicular to the laser pulse propagation direction. Here α is the convergence angle, $\lambda = 800$ nm is the fundamental laser wavelength. In the simulations, we considered the initial temperature distribution

$$T_0(x, y) = T_{00} \exp\left(-\frac{x^2 + y^2}{a_{fil}^2}\right) \times (1 + \cos[kx \sin \alpha]) , \tag{17.9}$$

where $T_{00} = 70$ K and $k = 2\pi/\lambda$ is a wavenumber. The angle α between the propagation axes of the two noncollinearly converging beams was varied between 0 and 2°, therefore the minimum grating period studied $d_{pl} \approx 23$ μm.

The grid step in the temporal domain was linked to the spatial grid size through the Courant condition

$$\frac{c_\mathrm{m}\,\delta t}{\delta x} + \frac{c_\mathrm{m}\,\delta t}{\delta y} \leq 1\ , \tag{17.10}$$

where c_m is the maximal velocity (17.5) over the (x, y) domain.

The solution to the wave equation (17.3) with the initial temperature perturbation (17.9) is represented by the waveform $\xi(x, y, t)$. The simulation results presented in Sect. 17.3 show the distributions of $\rho'(x, y)$ at the characteristic time moments. The cross sections along one of the transverse coordinates are provided. The Fourier transform is taken from the waveform at the chosen cross sections for the analysis of the waveform spatial scales.

17.3 Plasma Grating Characterization by Acoustic Waveform and Its Spectrum

The free electrons produced by the two converging beams overlapping in the geometrical focus recombine with the parent ions and disturb the flat background temperature

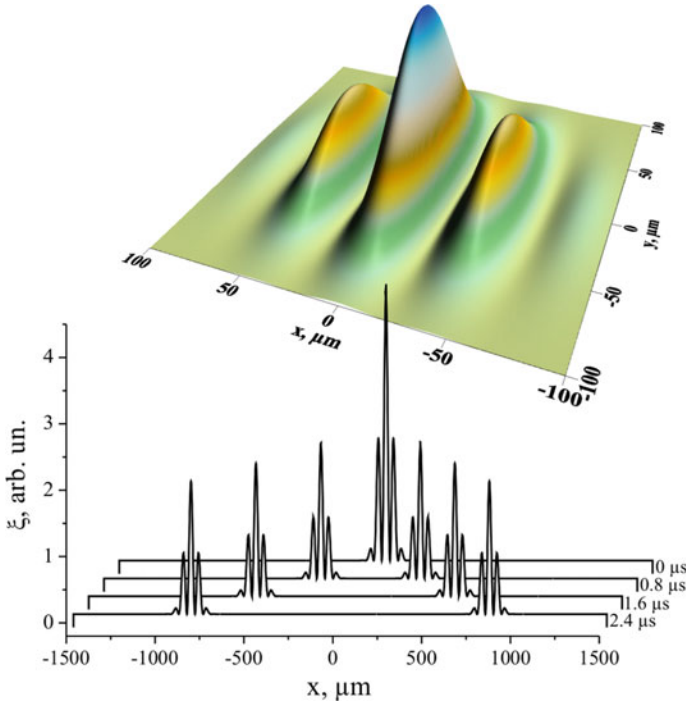

Fig. 17.1 (Upper panel) Temperature profile of the medium $T_0(x, y)$ after recombination of the plasma grating produced by the two 800-nm beams converging at an angle $\alpha = 1°$. (Lower panel) The solution of one-dimensional wave equation for the initial conditions $T_0(x, y = 0)$ from the upper panel

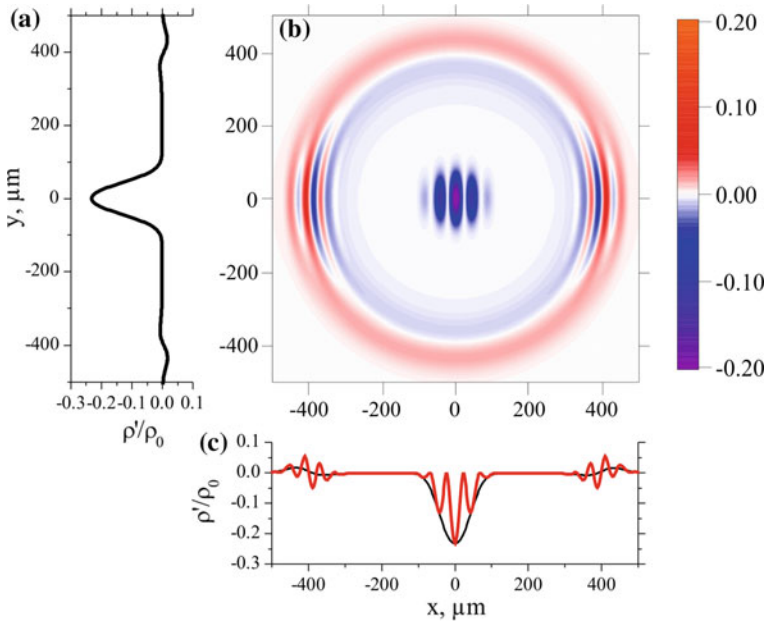

Fig. 17.2 **a**, **c** Air density perturbation $\rho'(x, y)/\rho_0$ cross sections at the time moment $t = 1.2\,\mu$s after the ionizing laser pulse. The black solid line in panel (**c**) is the same as in panel (**a**) and shows isotropic waveform for the reference. **b** The two-dimensional distribution of the acoustic waveform in the plane perpendicular to the laser pulse propagation direction

profile θ_0. The resulting temperature perturbation $T_0(x, y)$ is given by (17.9) and is shown in the upper panel of Fig. 17.1 at the time moment $t = 0$. The temperature perturbation at the zero time moment is directly proportional to the medium excitation function $\xi(x, y, t = 0)$, since $\rho' = 0$, see (17.4). With the time, the excitation $\xi(x, y, t)$ travels away from the source. By considering one-dimensional excitation $\xi(x, t)$, we obtain motion of the two waveforms in the opposite directions along the x-axis with the velocities of ± 340 m/s (the lower panel of Fig. 17.1).

In the two-dimensional simulations the medium excitation function $\xi(x, y, t)$ is represented by the superposition of the two waves: the isotropic cylindrical one surrounding the overall extended plasma channel and the wave directed along the plasma grating. The medium density perturbation $\rho'(x, y, t)$ is recalculated from the excitation function $\xi(x, y, t)$ according to (17.4) and plotted in the transverse (x, y) plane as the color map (Fig. 17.2b) and the cross sections in the direction perpendicular (Fig. 17.2a) and parallel (Fig. 17.2c) to the plasma grating at the time moment $t = 1.2\,\mu$s after the initial femtosecond laser pulse producing the filament.

Analysis of the plasma grating can be performed based on the acoustic signals, which can be detected in either parallel (x-axis) or perpendicular (y-axis) direction with respect to the axis of plasma grating modulation (Fig. 17.3a, compare red and black solid curves). In x-direction parallel to the grating orientation the signal wave-

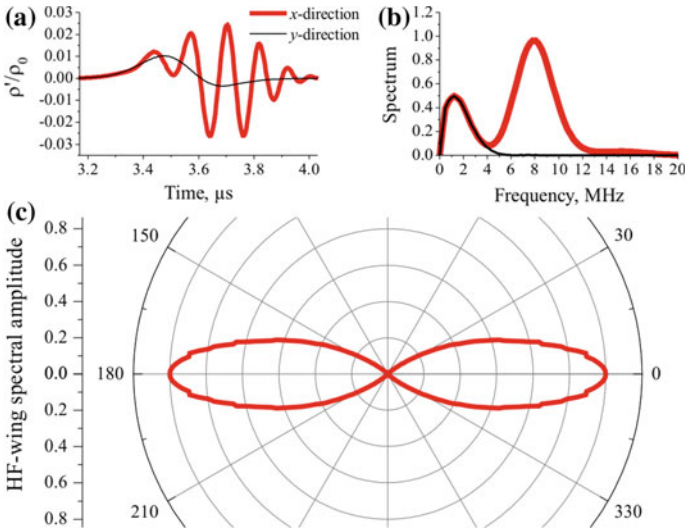

Fig. 17.3 **a** The acoustic signal waveforms detected in the x- and y-axes directions (red and black, respectively). **b** The corresponding spectra of the acoustic signals. **c** The polar plot of the acoustic signal spectral amplitude at 8 MHz, i.e. the directional diagram of the higher-frequency part of acoustic waveform spectrum

form exhibits two characteristic temporal scales: the larger one corresponding to the overall transverse plasma grating size and equal to 0.5 μs, that is 340 m/s × 0.5 μs = 170 μm in the transverse spatial domain, and the smaller one corresponding to the plasma grating period and equal to 0.125 μs or 340 m/s × 0.125 μs = 42.5 μm (red solid curve in Fig. 17.3a). Just a single-cycle waveform is obtained in the y-direction perpendicular to the grating orientation (black solid curve in Fig. 17.3a). The spectral analysis of the two waveforms propagating in the perpendicular directions shows the specific acoustic wave frequencies of 2 MHz and 8 MHz corresponding to the larger and smaller plasma grating spatial scales (Fig. 17.3b, red and black solid curves), respectively. The directional diagram of acoustic signal filtered at 8 MHz shows a factor of 1.4 amplitude decrease within 2 × 15° = 30° relative to the plasma grating parallel axis (the x-axis) (Fig. 17.3c). This means that half of the high-frequency signal energy propagates along the plasma grating and almost zero of this signal energy propagates perpendicular to the plasma grating including the wide sector 30–150°. The low-frequency component propagates uniformly into the cylinder extended along the z-axis, which is the initial femtosecond pulse propagation axis (Fig. 17.2b). Thus, our dynamic plasma grating produced by the two colliding filaments is anisotropic source of acoustic waves and simultaneously the unique source of the directed higher-frequency acoustic wave (Figs. 17.2b and 17.3c).

The transverse size of converging filaments in the vicinity of the geometrical focus (100−200 μm) is much larger than the plasma grating period (20−40 μm). Therefore, the interference pattern of the two beams is similar to that of the two

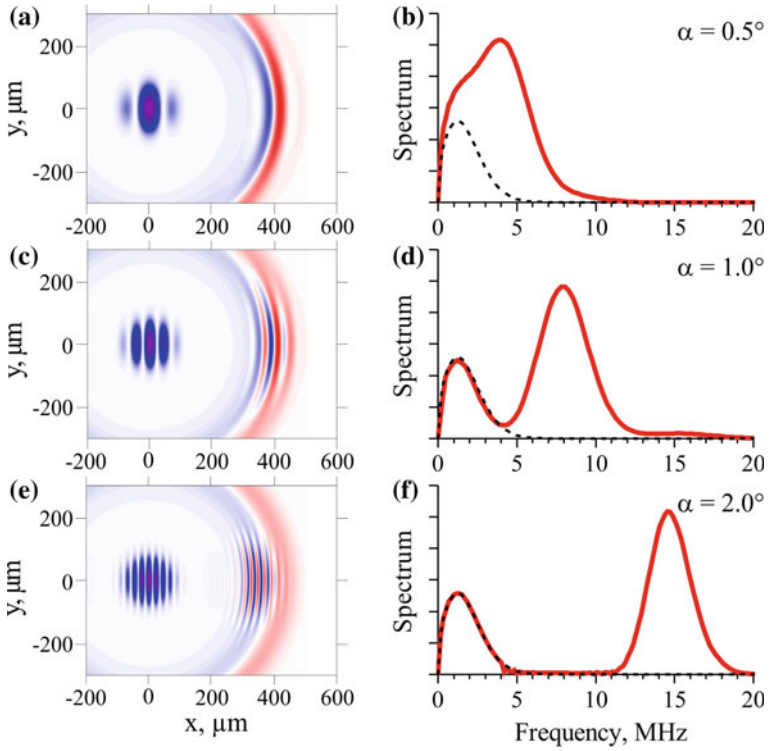

Fig. 17.4 (Left column) The transverse distribution of the air density perturbation $\rho'(x, y)/\rho_0$ at the time moment $t = 1.2\,\mu$s after plasma has recombined and (right column) the corresponding spectra from the plasma grating formed by filaments converging at **a**, **b** 0.5°, **c**, **d** 1° and **e**, **f** 2°. Black line in (**b**, **d**, **f**) is an isotropic part of the signal, which is the same for all the converging angles α studied

plane waves converging at a small angle of several degrees or less than that. We can introduce the characteristic frequencies for acoustic waveforms:

$$f_{\rm pl} = \frac{c_0}{d_{\rm pl}} = \frac{c_0 \sin\alpha}{\lambda}; \qquad f_{\rm fil} = \frac{c_0}{d} = \frac{c_0}{2a_{\rm fil}}\,. \tag{17.11}$$

The exact angle of convergence can be reconstructed from the frequency $f_{\rm pl}$ obtained from the waveform spectrum (Fig. 17.4a, c, e). By increasing the convergence angle α we decrease the period of the plasma grating $d_{\rm pl}$ and increase the frequency $f_{\rm pl}$ given by (17.8), (17.11). Because the overall transverse size of converging filaments remains the same, the lower frequency $f_{\rm fil}$ of the isotropic cylindrical acoustic wave corresponding to approximately 170 μm results in the spectral maximum at 2 MHz (Fig. 17.4b, d, f). The higher frequency $f_{\rm pl}$ of the acoustic wave propagating par-

allel to the plasma grating increases from 4 to 15 MHz according to (17.11) as the convergence angle increases from 0.5 to 2°.

The suggested noninvasive method for the plasma grating period and beam convergence angle detection can be realized as follows. A wideband piezoelectric transducer [15, 16] is translated along the propagation axis z at a distance of several millimeters from the plasma channel in order to detect the exact position of the maximum acoustic signal. Then, at the z-position with the maximum signal, the transducer is rotated in the transverse (x, y) plane with the purpose to find the maximum high-frequency signal irradiated by the plasma grating. The detected waveforms are Fourier transformed and the amplitude of the high-frequency maximum position is identified. The direction, at which the higher-frequency spectral component takes its maximum, is the x-axis or parallel axis of the plasma grating (Fig. 17.3c).

As soon as the plasma grating axis is identified, the convergence angle may be varied and the higher-frequency spectral maximum position is changed accordingly as shown in Fig. 17.4b, d, f. The higher frequency is inversely proportional to the plasma grating period in agreement with (17.11).

17.4 Conclusions

In this paper we have designed the physical model and numerical algorithm for the simulations of acoustic wave propagation from the source induced by the femtosecond plasma grating relaxation in atmospheric air. The model is based on the wave equation with the wave velocity depending on the transverse temperature variation. The numerical grid has the size of $4 \times 4\,\text{mm}^2$ and resolution of about 2 μm. The grid is aimed at the description of the fine plasma channel substructures in the course of femtosecond filamentation.

We have shown that the femtosecond plasma grating emits the superposition of two acoustic signals after plasma recombination. One acoustic signal is represented by an isotropic cylindrical waveform with the characteristic spatial scale equal to the filament diameter in the range 100−200 μm. The other acoustic signal is the wave with the characteristics spatial scale equal to the plasma grating period in the range 20−40 μm. This second wave propagates almost parallel to the plasma grating axis. The directional diagram corresponds to 50% energy of high-frequency wave localized within 30° angle (±15° from the plasma grating parallel axis).

The presence of the two characteristic spatial scales in the acoustic signal from the plasma grating is readily recognized in the acoustics signal spectrum. The spectrum reveals the maxima at two frequencies: the first one at approximately 2 MHz corresponds to ∼170 μm of the overall filament diameter, the second one increases from 4 to 15 MHz as the convergence angle increases from 0.5 to 2°.

We suggested the noninvasive method for the plasma grating period and beam convergence angle detection. The method is based on the translation of a wideband (more than 6 MHz) piezoelectric transducer along the pulse propagation axis in order to detect the exact z-position of the maximum acoustic signal. Then, at the z-position with the maximum signal, the transducer is rotated in the (x, y) plane and the plasma

grating parallel axis is revealed as the direction at which the higher frequency spectral component takes its maximum value. The value of this higher frequency itself is the inverse period of the plasma grating multiplied by the speed of sound in air.

Acknowledgements This work was partially supported by the Russian Foundation for Basic Research (Grant Nos. 18-52-16020, 18-02-00954, 18-32-01000) and the National key research and development program (2018YFB0504400). D.E.S. acknowledges the program "UMNIK" of Foundation of assistance to development of small forms of enterprises in scientific-technical sphere (FASIE) (11522GU/2017), Scholarship of "Basis" Foundation, Scholarship of RF President SP-2453.2018.2, and SPIE 2018 Optics and Photonics Education Scholarship.

References

1. S.L. Chin, S.A. Hosseini, W. Liu, Q. Luo, F. Theberge, N. Akozbek, A. Becker, V.P. Kandidov, O.G. Kosareva, H. Schroeder, Can. J. Phys. **83**, 863 (2005)
2. A. Couairon, A. Mysyrowicz, Phys. Rep. **441**, 47 (2007)
3. V.P. Kandidov, S.A. Shlenov, O.G. Kosareva, Quant. Electron. **39**, 205 (2009)
4. S.L. Chin, N. Akozbek, A. Proulx, S. Petit, C.M. Bowden, Opt. Comm. **188**, 181–186 (2001)
5. Y. Chen, F. Théberge, O. Kosareva, N. Panov, V.P. Kandidov, S.L. Chin, Opt. Lett. **32**, 3477–3479 (2007)
6. W. Liu, S.A. Hosseini, Q. Luo, B. Ferland, S.L. Chin, O.G. Kosareva, N.A. Panov, V.P. Kandidov, New J. Phys. **6**, 6 (2004)
7. D. Uryupina, M. Kurilova, A. Mazhorova, N. Panov, R. Volkov, S. Gorgutsa, O. Kosareva, A. Savel'ev, S.L. Chin, J. Opt. Soc. Am. B **27**, 667–674 (2010)
8. S.A. Hosseini, Q. Luo, B. Ferland, W. Liu, N. Akozbek, G. Roy, S.L. Chin, Appl. Phys. B **77**, 697–702 (2003)
9. Q. Luo, W. Liu, S.L. Chin, Appl. Phys. B **76**, 337–340 (2003)
10. J. Yu, D. Mondelain, J. Kasparian, E. Salmon, S. Geffroy, C. Favre, V. Boutou, J.-P. Wolf, Appl. Opt. **42**, 7117 (2003)
11. D.V. Kartashov, A.V. Kirsanov, A.M. Kiselev, A.N. Stepanov, N.N. Bochkarev, Y.N. Ponomarev, B.A. Tikhomirov, Opt. Express **14**, 7552 (2006)
12. J.K. Wahlstrand, N. Jhajj, E.W. Rosenthal, S. Zahedpour, H.M. Milchberg, Opt. Lett. **39**, 1290–1293 (2014)
13. K.P. Birch, J. Opt. Soc. Am. A **8**, 647–651 (1991)
14. N. Jhajj, E.W. Rosenthal, R. Birnbaum, J.K. Wahlstrand, H.M. Milchberg, Phys. Rev. X **4**, 011027 (2014)
15. D.S. Uryupina, A.S. Bychkov, D.V. Pushkarev, E.V. Mitina, A.B. Savel'ev, O.G. Kosareva, N.A. Panov, A.A. Karabutov, E.B. Cherepetskaya, Laser Phys. Lett. **13**, 095401 (2016)
16. A.S. Bychkov, E.B. Cherepetskaya, A.A. Karabutov, V.A. Makarov, Laser Phys. Lett. **13**, 085401 (2016)
17. V.G. Andreev, A.A. Karabutov, S.V. Solomatin, E.V. Savateeva, V. Aleinikov, Yu.V. Zhulina, R.D. Fleming, A.A. Oraevsky, Proc. SPIE **3916**, 36 (2000)
18. E.W. Rosenthal, N. Jhajj, I. Larkin, S. Zahedpour, J.K. Wahlstrand, H.M. Milchberg, Opt. Lett. **41**, 3908–3911 (2016)
19. G. Point, E. Thouin, A. Mysyrowicz, A. Houard, Opt. Express **24**, 6271–6282 (2016)
20. D.V. Pushkarev, E.V. Mitina, D.S. Uryupina, R.V. Volkov, N.A. Panov, A.A. Karabutov, O.G. Kosareva, A.B. Savel'ev, JETP Lett. **106**, 561–564 (2017)
21. S. Tzortzakis, B. Prade, M. Franco, A. Mysyrowicz, Opt. Commun. **181**, 123 (2000)
22. S. Xu, Y. Zheng, Y. Liu, W. Liu, Laser Phys. **20**, 1968–1972 (2010)
23. V.V. Pankratov, D.E. Shipilo, M.M. Yandulsky, N.A. Panov, O.G. Kosareva, Proc. SPIE **9990**, 99900N–1 (2016)